Interdisciplinary Materials

WILEY

Interdisciplinary Materials — Open Access

RESEARCH ARTICLE OPEN ACCESS

Leveraging Atomic Disorder to Modulate Hydrogen Storage Thermodynamics in Intermetallics

Yuanyuan Shang[1] | Ting Chen[2] | Zhifeng Lei[3] | Archa Santhosh[1] | Paul Jerabek[1] | Benjamin Klusemann[2,4] | Zhaoping Lu[5] | Thomas Klassen[1,6] | Claudio Pistidda[1]

[1]Materials Design, Institute of Hydrogen Technology, Helmholtz-Zentrum Hereon, Geesthacht, Germany | [2]Solid State Materials Processing, Institute of Material and Process Design, Helmholtz-Zentrum Hereon, Geesthacht, Germany | [3]College of Materials Science and Engineering, Hunan University, Changsha, China | [4]Institute for Production Technology and Systems, Leuphana University Lüneburg, Lüneburg, Germany | [5]Beijing Advanced Innovation Center for Materials Genome Engineering, State Key Laboratory for Advanced Metals and Materials, University of Science and Technology Beijing, Beijing, China | [6]Department of Mechanical and Civil Engineering, Helmut Schmidt University, Hamburg, Germany

Correspondence: Zhifeng Lei (zflei@hnu.edu.cn) | Zhaoping Lu (luzp@ustb.edu.cn) | Claudio Pistidda (claudio.pistidda@hereon.de)

Received: 20 October 2025 | **Revised:** 10 December 2025 | **Accepted:** 24 December 2025

Keywords: compositionally complex intermetallics | density functional theory calculations | functional properties | hydrogen storage materials

ABSTRACT

Hydrogen storage in metal hydrides holds great promise for advancing a low-carbon energy future. Yet, fine-tuning the thermodynamics of hydrogen absorption remains challenging with traditional microalloying approaches. Here, we report a strategy inspired by compositionally complex alloy design to introduce atomic disorder into the prototypical TiFe intermetallic system. By progressively substituting Fe with Co, Ni, Cu, and Mn in equal proportions, we synthesize a series of near-single-phase *B2*-structured compositionally complex intermetallics, that is, $Ti_{50}(FeCo)_{50}$, $Ti_{50}(FeCoNi)_{50}$, $Ti_{50}(FeCoNiCu)_{50}$, and $Ti_{50}(FeCoNiCuMn)_{50}$ (at.%). These materials exhibit hydrogen storage capacities (measured by pressure-composition isotherm, PCI) of 1.39, 1.42, 1.31, and 1.14 wt.% under 100 bar of H_2 at 50°C, respectively. Notably, $Ti_{50}(FeCo)_{50}$ demonstrates rapid hydrogen uptake kinetics, achieving 90% of its full capacity within 77 s under 50 bar of hydrogen pressure at 50°C. Hydrogen storage thermodynamic analyses reveal that increasing atomic disorder stabilizes the hydride phase, with thermodynamic stability following the order: $Ti_{50}(FeCoNiCuMn)_{50} > Ti_{50}(FeCoNi)_{50} > Ti_{50}(FeCoNiCu)_{50} > Ti_{50}(FeCo)_{50}$. Our findings establish atomic disorder as a versatile thermodynamic tuning knob for intermetallic hydrides, offering a rational framework for the design of advanced hydrogen storage materials.

1 | Introduction

Hydrogen is widely regarded as a pivotal energy carrier in the transition to a carbon-neutral future, owing to its exceptional gravimetric energy density (~120 MJ kg^{-1}), which surpasses that of conventional fuels such as methane, propane, and gasoline [1]. However, the widespread adoption of hydrogen is greatly hindered by challenges associated with its storage and transport. Among the various storage strategies, solid-state hydrogen storage offers distinct advantages, including high energy density, intrinsic safety, and minimal energy loss, making it particularly attractive for stationary applications [2–5]. Room-temperature metal hydrides have emerged as promising candidates, owing to their favorable thermodynamics and moderate operating conditions [6, 7]. Notably, the *B2*-type intermetallic compound TiFe can reversibly store ca. 1.33 wt.% of hydrogen within 10 min under 65 bar of H_2 at 40°C, demonstrating low-pressure operation, efficient thermal management and rapid kinetics [8]. These features position TiFe as a viable material for practical deployment. However, its hydrogen storage performance remains suboptimal. Achieving further improvements requires a holistic design strategy that integrates considerations of activation behavior, storage capacity, thermodynamic stability, and kinetic performance.

Traditional approaches to tuning metal hydride properties have relied heavily on microalloying or processing modifications. For example, the introduction of 4 at.% Cr into TiFe simplifies activation, requiring only 20 to 24 h under 25 bar of H_2 at 300°C, but it reduces the storage capacity to 1.0 wt.% under 60 bar of H_2 at 22°C [9]. Substitution of 0.1 at.% Ni for Fe in TiFe dramatically enhances kinetics, yielding 0.9 wt.% uptake within 5 min under 30 bar of H_2 at 40°C, yet widens the pressure gap between the first and second plateaus and thus diminishes reversible capacity [10, 11]. Mn emerges as a particularly effective modifier: replacing 10 at.% Fe with Mn increases the reversible capacity from 1.31 to 1.50 wt.% at 25°C under a pressure range of 0.3 to 25 bar of H_2, albeit at the cost of a steeper plateau slope and broader operating pressure range [12]. Similarly, ball milling, ion implantation, and severe deformation markedly improve activation but incur capacity penalties [13–15]. For instance, milling the as-cast TiFe-based intermetallic for 60 min reduces its capacity from 1.39 to 1.05 wt.% under 35 bar of H_2 at 50°C [16].

Compositionally complex alloys have recently attracted considerable attention for energy-related applications, owing to their vast compositional diversity and highly tunable properties [17–25]. Comprising multiple principal elements in near-equiatomic ratios, compositionally complex alloys introduce substantial atomic disorder into the crystal lattice, profoundly influencing structural and chemical behavior. This intrinsic disorder offers a wide range of possibilities to tune the hydrogen storage properties in the desired direction, which offers new opportunities to engineer hydrogen storage behavior in ways not possible with conventional alloys. For instance, Dangwal et al. developed a compositionally complex alloy with AB-type configuration, that is, $TiV_2ZrCrMnFeNi$ alloy with dual C14 Laves and body-centered cubic (bcc) phases [26]. The results show that the main phase for hydrogenation is the C14 phase, while the existence of the bcc phase helps to build the interphase boundaries, thus promoting the activation behavior of the alloy. The $TiV_2ZrCrMnFeNi$ alloy can reversibly absorb/desorb 1.6 wt.% of hydrogen at 20°C under a pressure of 100 bar of H_2, as obtained from pressure-composition isotherm (PCI) curves. The kinetic results show that the hydrogenation reaches a steady state within 1 min, suggesting fast kinetic behavior. Later on, with the support of machine learning method, a series of $Ti_xZr_{2-x}CrMnFeNi$ ($x = 0.5$, 1.0, and 1.5) with desired enthalpy for room-temperature hydrogen storage were developed [27]. The hydride formation enthalpies of these predicated alloys fall well in the range of −39 to −25 kJ mol^{-1}, which are in good agreement with the experimental and density functional theory (DFT) calculations data. The findings suggest that machine learning can serve as an efficient and dependable tool for designing compositionally complex alloys with tailored hydrogen storage characteristics.

Inspired by the design principles of compositionally complex alloys, we substitute Fe with Co, Ni, Cu, and Mn in equiatomic ratios to introduce atomic disorder into the prototypical TiFe intermetallic system. $Ti_{50}(FeCo)_{50}$ was selected as the starting composition since Ti-Co and Fe-Co pairs have favorable mixing enthalpies, indicating a thermodynamically stable and homogeneous intermetallic phase. This provides a well-defined structural and thermodynamic stability for systematically studying atomic disorder by compositionally complex alloying on the B sites. The resulting compositionally complex intermetallics (CCIs) $Ti_{50}(FeCo)_{50}$, $Ti_{50}(FeCoNi)_{50}$, $Ti_{50}(FeCoNiCu)_{50}$, and $Ti_{50}(FeCoNiCuMn)_{50}$ (at.%) all adopt a predominantly single *B2*-ordered phase structure, yet display markedly different kinetic and thermodynamic responses upon hydrogen uptake. These CCIs reversibly absorb 1.39, 1.42, 1.31, and 1.14 wt.% of hydrogen, respectively, under 100 bar of H_2 at 50°C. Their corresponding hydrogenation plateau pressures at 100°C are 4.21, 0.47, 0.73, and 0.44 bar, highlighting the tunable thermodynamics achieved through controlled compositional complexity. This atomic disorder-driven design paradigm opens new avenues for engineering advanced hydrogen storage materials with tailored performance.

2 | Results and Discussion

2.1 | Microstructural Characterization

We used synchrotron radiation powder X-ray diffraction (SR-PXD) to investigate the crystal structures of $Ti_{50}(FeCo)_{50}$, $Ti_{50}(FeCoNi)_{50}$, $Ti_{50}(FeCoNiCu)_{50}$, and $Ti_{50}(FeCoNiCuMn)_{50}$ CCIs (Figure 1A–D). All four CCIs exhibit a nearly single-phase *B2* structure, which has an ordered bcc lattice (space group $Pm\bar{3}m$). Their calculated lattice constants are 2.9875 ± 0.0001, 3.0047 ± 0.0001, 3.0275 ± 0.0003, and 3.0256 ± 0.0001 Å, respectively. As the number of alloying elements increases from $Ti_{50}(FeCo)_{50}$ to $Ti_{50}(FeCoNiCu)_{50}$, the lattice expands accordingly. However, the addition of Mn in $Ti_{50}(FeCoNiCuMn)_{50}$ does not further increase the lattice constant, suggesting that the influence of configurational entropy on lattice expansion diminishes beyond a certain compositional complexity. Despite the slight changes in lattice constant, all CCIs retain the same *B2* structure as $Ti_{50}Fe_{50}$ (lattice constant $a = 2.9788 \pm 0.0004$ Å), with only trace amounts of Ti_2Fe-type secondary phase detected [8]. All CCIs possess larger lattice constants than $Ti_{50}Fe_{50}$, indicating that the introduction of multiple elements leads to lattice expansion. Rietveld refinement reveals that the secondary phase content in all four CCIs is negligible, remaining below 1 wt.%, see Figures S1–S4. In the case of $Ti_{50}Fe_{50}$, cap. 1.4 ± 0.1% of the Ti_2Fe phase was detected. When synthesized using the same protocol (arc melting, casting, and crushing), CCIs exhibit phase constitutions comparable to those of $Ti_{50}Fe_{50}$ intermetallics. Figure 1E–H show the atomic configurations generated using the special quasi-random structure (SQS) model. Each model contains 128 atoms. As more elements are introduced, the degree of atomic disorder increases, reflecting the growing chemical complexity of the system.

The microstructures of all four CCIs were further investigated by scanning electron microscopy (SEM), energy-dispersive X-ray spectroscopy (EDS), and electron backscatter diffraction (EBSD). Figure 2A,B display the SEM micrographs of the as-cast $Ti_{50}(FeCo)_{50}$ CCI. SEM reveals a uniform *B2* matrix punctuated by sparse, submicron particles at grain boundaries. EDS, in conjunction with SR-PXD, identifies these particles as the $Ti_2(FeCo)$ phase (Figure S5). EBSD mappings (Figure 2C,D) yield an average grain size of 12.6 μm for this CCI. Figure 2E,F,I,J,M,N show analogous micrographs for $Ti_{50}(FeCoNi)_{50}$, $Ti_{50}(FeCoNiCu)_{50}$, and

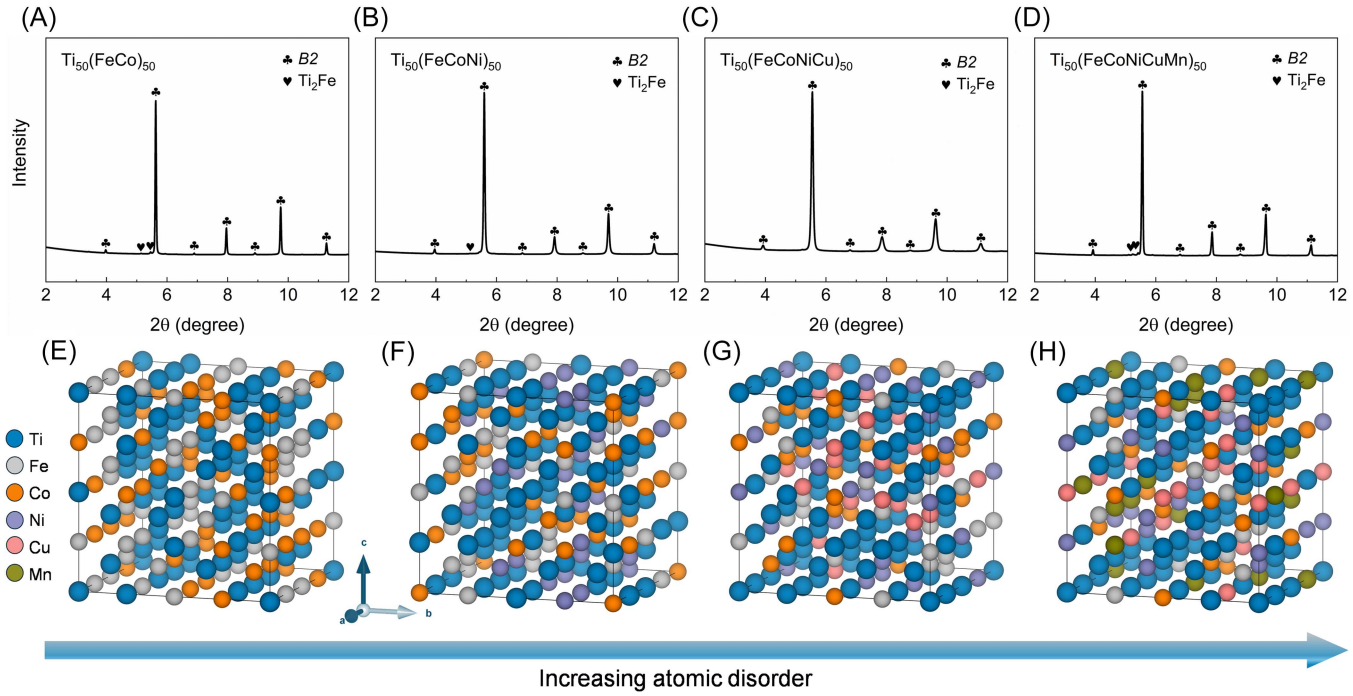

FIGURE 1 | Crystallographic features. (A–D) SR-PXD patterns of $Ti_{50}(FeCo)_{50}$, $Ti_{50}(FeCoNi)_{50}$, $Ti_{50}(FeCoNiCu)_{50}$, and $Ti_{50}(FeCoNiCuMn)_{50}$ CCIs (wavelength $\lambda = 0.20735$ Å), illustrating phase evolution with increasing atomic disorder. (E–H) Corresponding atomic configurations generated via the SQS approach, revealing local structural motifs and atomic disorder across the CCI series.

$Ti_{50}(FeCoNiCuMn)_{50}$, respectively. In all cases, the *B2* phase dominates, with only trace secondary phases surrounding grain boundaries. Elemental distributions (Figures S5,S6) reveal that in both $Ti_{50}(FeCo)_{50}$ and $Ti_{50}(FeCoNi)_{50}$, Co and Ni occupy mainly Fe sites, leaving Ti at ~50 at.% in the *B2* matrix. In $Ti_{50}(FeCoNiCu)_{50}$, however, the *B2* matrix contains ~40 at.% Ti and ~30 at.% Cu (Figure S7), indicating that Cu substitutes for both Fe and Ti sites. In the *B2* matrix of $Ti_{50}(FeCoNiCuMn)_{50}$, Ti remains at ~40 at.% and Cu at ~20 at.% (Figure S8), suggesting that Mn preferentially occupies Fe sites while Cu distributes over both Fe and Ti positions. The secondary phases also evolve with composition. The grain-boundary phase in $Ti_{50}(FeCoNi)_{50}$ corresponds to $Ti_2(FeCoNi)$ (Figure S6G). In $Ti_{50}(FeCoNiCu)_{50}$, this phase shows a Ti:(Co + Ni + Cu) ratio of ca. 4:1, reflecting its Ti enrichment and Cu depletion (Figure S7H). In $Ti_{50}(FeCoNiCuMn)_{50}$, EDS line-scan indicates a Ti:(Co + Ni + Cu + Mn) ratio near 2:1, akin to the secondary phases in $Ti_{50}(FeCo)_{50}$ and $Ti_{50}(FeCoNi)_{50}$ (Figure S8I). This progression highlights Cu's pronounced role in secondary-phase formation. EBSD measurements (Figure 2G,H,K,L,O,P) show that $Ti_{50}(FeCoNi)_{50}$ grains average 12.6 μm, which is comparable to $Ti_{50}(FeCo)_{50}$. The grain sizes for $Ti_{50}(FeCoNiCu)_{50}$ and $Ti_{50}(FeCoNiCuMn)_{50}$ refine to 7.1 and 7.9 μm, respectively. Despite increasing chemical complexity, the average grain size remains primarily governed by the presence of Cu, rather than configurational entropy. As a matter of comparison, the average grain size for the $Ti_{50}Fe_{50}$ intermetallic prepared by the same method is approximately 41.0 μm, as shown in Figure S9, which is about three to five times as large as those of the four CCIs investigated here. The results imply that multi-elemental substitution leads to a significant reduction in grain size, which may influence the hydrogen diffusion pathways and nucleation sites for the hydride phase.

2.2 | Hydrogen Storage Properties

Figure 3A,E,I,M present PCIs from 0 to 100 bar for all four CCIs. Expanded views from 0 to 15 bar appear in Figure 3B,F,J,N. At 50°C under 100 bar of H_2, $Ti_{50}(FeCo)_{50}$, $Ti_{50}(FeCoNi)_{50}$, $Ti_{50}(FeCoNiCu)_{50}$, and $Ti_{50}(FeCoNiCuMn)_{50}$ reach hydrogen storage capacities of 1.39, 1.42, 1.31, and 1.14 wt.%, respectively. The plateau pressures were determined by identifying the midpoint of each plateau region on the PCIs. $Ti_{50}(FeCo)_{50}$ exhibits a two-step hydrogenation: at 50°C, the first and second hydrogenation plateaus lie at 0.39 and 8.59 bar (dehydrogenation at 0.26 and 8.21 bar), which shift to 4.21/25.41 bar (hydrogenation) and 3.31/19.90 bar (dehydrogenation) at 100°C. van't Hoff fittings of the first plateau over 50°C–125°C yield the hydrogenation enthalpy $\Delta H_{abs} = -47.5 \pm 0.4$ kJ mol^{-1}, hydrogenation entropy $\Delta S_{abs} = -139.1 \pm 1.1$ J K^{-1} mol^{-1} (Figure 3C), dehydrogenation enthalpy $\Delta H_{des} = 49.7 \pm 1.0$ kJ mol^{-1}, and dehydrogenation entropy $\Delta S_{des} = 142.9 \pm 2.7$ J K^{-1} mol^{-1} (Figure 3D). In contrast, $Ti_{50}(FeCoNi)_{50}$ displays a single plateau at ~0.02 bar for both hydrogenation and dehydrogenation process at 50°C, shifting to 0.47/0.41 bar at 100°C. Its thermodynamics over 50°C–200°C gives $\Delta H_{abs} = -55.1 \pm 4.5$ kJ mol^{-1}, $\Delta S_{abs} = -140.4 \pm 11.5$ J K^{-1} mol^{-1} (Figure 3G), $\Delta H_{des} = 53.8 \pm 4.7$ kJ mol^{-1} and $\Delta S_{des} = 136.1 \pm 12.3$ J K^{-1} mol^{-1} (Figure 3H). Substituting Cu in $Ti_{50}(FeCoNiCu)_{50}$ raises the 50°C plateau to 0.21 bar for hydrogenation (0.02 bar for dehydrogenation) and to 0.73/0.42 bar at 100°C. Its ΔH_{abs} and ΔS_{abs} drop to -34.5 ± 3.2 kJ mol^{-1} and $\Delta S_{abs} = -92.4 \pm 8.2$ J K^{-1} mol^{-1} (Figure 3K), with $\Delta H_{des} = 44.9 \pm 5.3$ kJ mol^{-1} and $\Delta S_{des} = 109.0 \pm 13.6$ J K^{-1} mol^{-1} (Figure 3L). Adding Mn restores stronger bonding, whereas $Ti_{50}(FeCoNiCuMn)_{50}$ shows at 50°C, both hydrogenation and dehydrogenation plateaus are 0.02 bar. The hydrogenation and dehydrogenation plateaus at 100°C are 0.44 and 0.11 bar, with $\Delta H_{abs} = -49.5 \pm 3.6$ kJ mol^{-1}, $\Delta S_{abs} = -122.9 \pm 9.2$

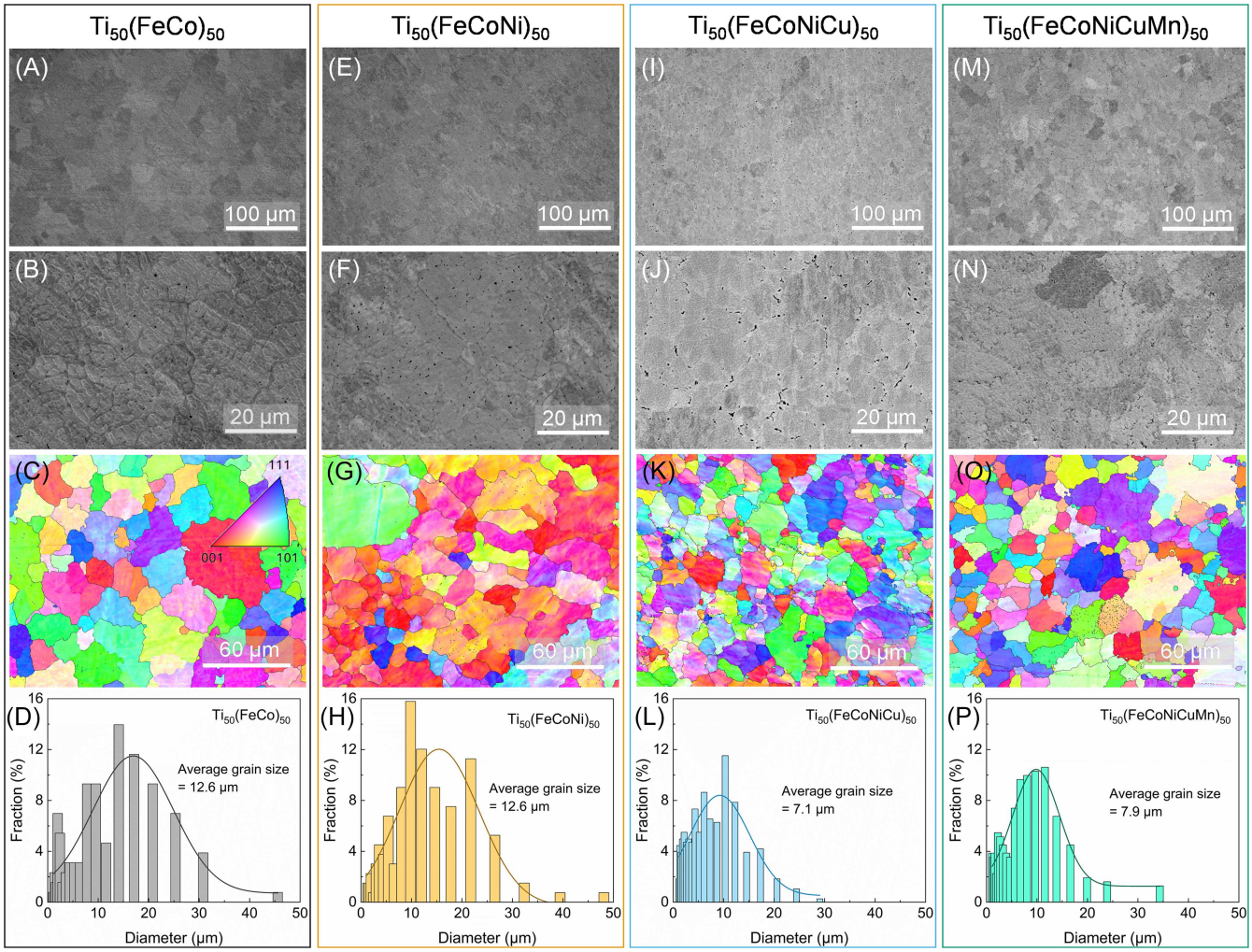

FIGURE 2 | Microstructural characteristics. (A–D) Secondary electron (SE) images, EBSD map, and crystallite size distribution of the $Ti_{50}(FeCo)_{50}$ CCI. (E–H) Corresponding SE images, EBSD map, and crystallite size distribution for $Ti_{50}(FeCoNi)_{50}$. (I–L) Microstructural analyses of $Ti_{50}(FeCoNiCu)_{50}$. (M–P) Microstructural analyses of $Ti_{50}(FeCoNiCuMn)_{50}$. The data highlight grain morphology, orientation, and size distribution across the CCI series as a function of increasing atomic disorder.

$J\,K^{-1}\ mol^{-1}$ (Figure 3O), $\Delta H_{des} = 50.0 \pm 5.4\,kJ\,mol^{-1}$, and $\Delta S_{des} = 120.3 \pm 14.1\,J\,K^{-1}\ mol^{-1}$ (Figure 3P). At 50°C, hydrogenation plateau pressures follow: $Ti_{50}(FeCo)_{50} > Ti_{50}(FeCoNiCu)_{50} > Ti_{50}(FeCoNi)_{50} = Ti_{50}(FeCoNiCuMn)_{50}$; at 100°C they rank: $Ti_{50}(FeCo)_{50} > Ti_{50}(FeCoNiCu)_{50} > Ti_{50}(FeCoNi)_{50} > Ti_{50}(FeCoNiCuMn)_{50}$. The CCI with more negative ΔH has a more negative ΔS value, for example, $Ti_{50}(FeCoNi)_{50}$ CCI has the most negative ΔH and ΔS. This is consistent with a ΔH-ΔS compensation behavior, which is frequently observed in metal–hydrogen systems. This compensation indicates that during the hydride formation process, the changes in metal–hydrogen bond strength are relatively offset by structural changes. Note that the binary TiFe system exhibits ΔH_{abs} of $-24.6\,kJ\,mol^{-1}$ H_2 and ΔS_{abs} of $-100.8\,J\,K^{-1}\ mol^{-1}$ H_2, which provides a useful reference point for assessing the role of chemical complexity [8]. The ΔS_{abs} values of $Ti_{50}(FeCo)_{50}$, $Ti_{50}(FeCoNi)_{50}$, and $Ti_{50}(FeCoNiCuMn)_{50}$ are more negative than that of binary TiFe, indicating that upon hydrogenation, hydrogen in these CCIs occupies various compositionally distinct local environments, resulting in greater loss of configurational freedom. In comparison, the $Ti_{50}(FeCoNiCu)_{50}$ CCI exhibits a less negative ΔS_{abs} than other CCIs and binary TiFe, implying that Cu not only modifies the bond strength of metal–hydrogen, but also reduces configurational contribution to the hydrogenation entropy. This suggests that some specific B site elements, such as Cu, can influence both hydrogenation enthalpy and entropy. The later introduction of Mn partly reestablishes stronger bonding and a more negative entropy, consistent with its analogous role to Co and Ni in the TiFe lattice. The hysteresis calculated from 100°C plateaus decreases from 1.20 in $Ti_{50}(FeCo)_{50}$ (first plateau only) to 0.85, 0.36, and 0.37 in the $Ti_{50}(FeCoNi)_{50}$, $Ti_{50}(FeCoNiCu)_{50}$, and $Ti_{50}(FeCoNiCuMn)_{50}$ CCIs, respectively. All four CCIs exhibit lower hysteresis than $Ti_{50}Fe_{50}$ (1.30), demonstrating more reversible hydride formation and tunable thermodynamics for practical hydrogen storage applications. It is worth noting that the observed hydrogenation/dehydrogenation thermodynamics are controlled not only by the hydrogen binding energy of individual elements, but also by the atomic disorder and related distribution of hydrogen binding local environment. On one hand, substituting Fe by Co, Ni, Cu, and Mn can modify the metal–hydrogen interactions due to their different hydrogen binding energies. In compositionally complex B sites, the substitutions can change the coordinates, electron densities, and local strains, thus altering the local

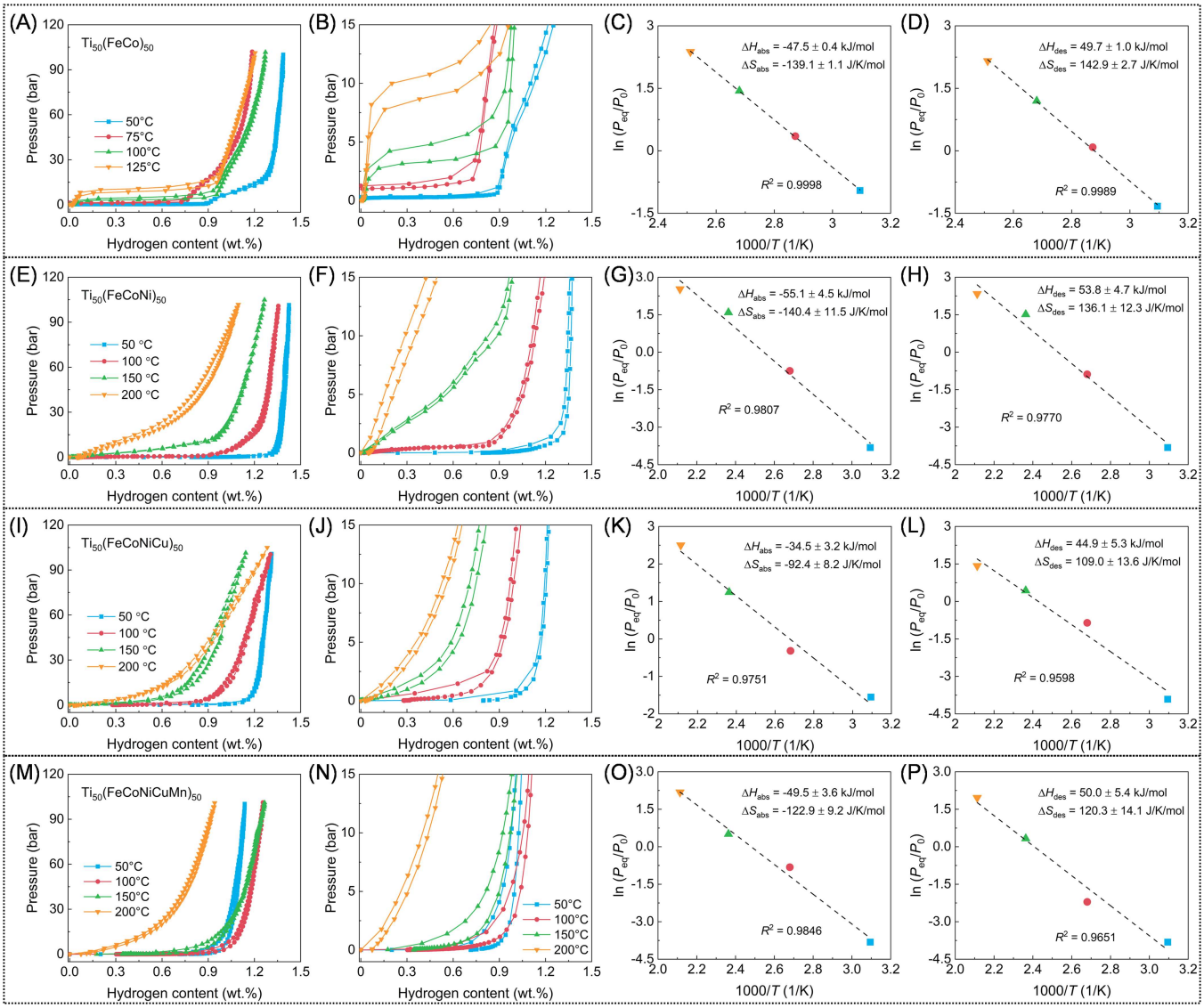

FIGURE 3 | Thermodynamic properties of hydrogen storage. (A–D) PCIs and van't Hoff analyses for determining the hydrogenation/dehydrogenation enthalpy (ΔH) and entropy (ΔS) of $Ti_{50}(FeCo)_{50}$. (E–H) Corresponding PCI curves and van't Hoff fittings for $Ti_{50}(FeCoNi)_{50}$. (I–L) Thermodynamic analyses of $Ti_{50}(FeCoNiCu)_{50}$. (M–P) Thermodynamic analyses of $Ti_{50}(FeCoNiCuMn)_{50}$. The results highlight systematic variations in hydrogen storage behavior and thermodynamic parameters with increasing atomic disorder.

chemical environment [28]. This can significantly affect the thermodynamic properties when compared to the binary TiFe alloy. On the other hand, the significance of introducing atomic disorder by compositionally complex alloying can lead to a broad distribution of hydrogen binding environments rather than a single characteristic environment [29, 30]. Therefore, the observed PCI plateau features are consistent with the broadened elemental distributions, which do not follow a simple linear or weighted-average relationship if we consider only the hydrogen binding energy of individual elements.

All CCIs require activation before PCI and kinetic measurements. Figure 4A,B show the first hydrogenation behaviors for the investigated CCIs under 65 bar of H_2 at 50°C. Compared to the binary $Ti_{50}Fe_{50}$ intermetallic, which takes about 150 h to activate, the newly designed CCIs activate much more quickly. In contrast, the $Ti_{50}(FeCoNi)_{50}$ CCI activates in 36.9 h, and the other three CCIs display even faster activation (Figure 4B). The $Ti_{50}(FeCoNiCuMn)_{50}$ CCI activates in 15 h, the $Ti_{50}(FeCo)_{50}$ CCI in 5 h, and the $Ti_{50}(FeCoNiCu)_{50}$ CCI in just 2.5 h, which is the quickest among all. These results highlight that atomic disorder introduced by multiple principal elements significantly improves activation behavior compared to the binary system. Following activation, dehydrogenation was performed under 0.5 bar of H_2 with a temperature range from 50°C to 300°C at 10°C min^{-1} (Figure 4C). The $Ti_{50}(FeCo)_{50}$ CCI delivers the highest capacity (1.44 wt.%), followed by $Ti_{50}(FeCoNi)_{50}$ (1.28 wt.%), $Ti_{50}(FeCoNiCuMn)_{50}$ (1.26 wt.%), and $Ti_{50}(FeCoNiCu)_{50}$ (1.03 wt.%). Notably, the $Ti_{50}(FeCo)_{50}$ CCI exhibits a rapid initial release of 0.51 wt.% of hydrogen. Hydrogenation kinetics were measured under 50 bar of H_2 at 50°C. The hydrogenation capacities for the $Ti_{50}(FeCo)_{50}$, $Ti_{50}(FeCoNi)_{50}$, $Ti_{50}(FeCoNiCu)_{50}$, and $Ti_{50}(FeCoNiCuMn)_{50}$ CCIs are 1.45, 1.33, 1.36, and 1.31 wt.%, respectively (Figure 4D). For comparison, the $Ti_{50}Fe_{50}$ intermetallic shows a hydrogenation capacity of 1.42 wt.% under the same

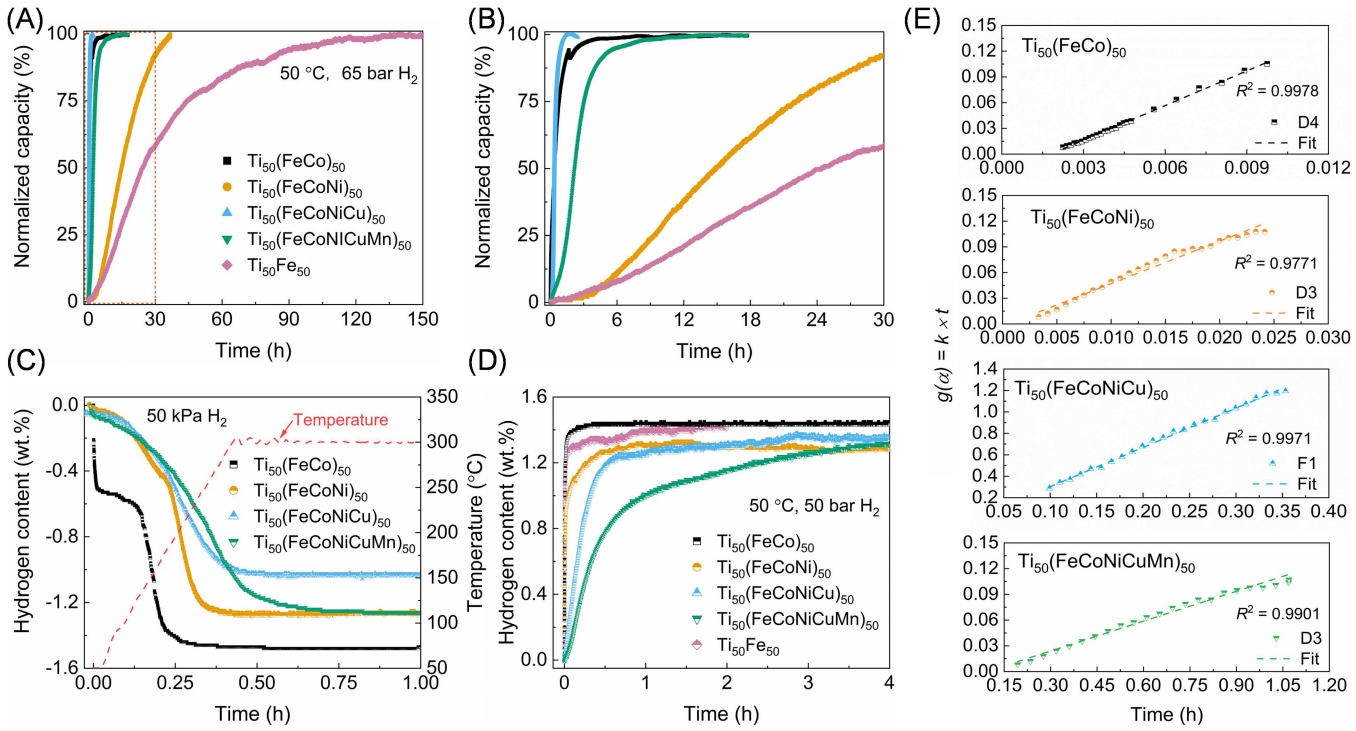

FIGURE 4 | Hydrogen storage kinetic properties. (A) First hydrogenation curves of $Ti_{50}(FeCo)_{50}$, $Ti_{50}(FeCoNi)_{50}$, $Ti_{50}(FeCoNiCu)_{50}$, and $Ti_{50}(FeCoNiCuMn)_{50}$ measured at 50°C under 65 bar of H_2. (B) Enlarged view of the initial hydrogenation stage (orange box in A). (C) Dehydrogenation kinetics under 0.5 bar back pressure with a temperature ramp from 50°C to 300°C at 10°C min^{-1}. (D) Comparative hydrogenation kinetics at 50°C under 50 bar of H_2. (E) Corresponding kinetic modeling results of the hydrogenation kinetics in (D). The results illustrate the influence of increasing atomic disorder on hydrogenation/dehydrogenation rates.

conditions. The $Ti_{50}(FeCo)_{50}$ CCI achieved 90% of its capacity (1.30 wt.%) within 77 s—significantly faster than the others, which required 1029, 2055, and 7845 s, respectively. The dehydrogenation rate trends mirror those of hydrogenation, underscoring the strong hydrogen-trapping effect introduced by high configurational entropy. These results indicate that increasing configurational entropy slows both dehydrogenation and hydrogenation, likely due to greater lattice distortion that hinders hydrogen diffusion. The Cu-alloyed $Ti_{50}(FeCoNiCu)_{50}$ exhibits a markedly faster activation than the other studied CCIs, yet its subsequent hydrogenation rate remains inferior to that of $Ti_{50}(FeCo)_{50}$ and $Ti_{50}(FeCoNi)_{50}$. All samples begin with comparable surface oxidation levels, but Cu introduction may lead to higher resistance to oxidation. This could influence the surface chemistry and passivation behavior, allowing more rapid oxide disruption and the emergence of fresh reactive sites during the initial hydrogenation process [31]. Simultaneously, the enlarged lattice constant in $Ti_{50}(FeCoNiCu)_{50}$ lowers the energy barrier for hydride nucleation, while hydrogen-induced microcracks and defects furnish additional heterogeneous nucleation centers [32]. These synergistic effects drive the accelerated activation, yet upon extended hydrogenation/dehydrogenation activities, the progressive defect accumulation, particle pulverization, and agglomeration affect the hydrogen diffusion pathways and ultimately diminish the kinetic advantage [33]. To elucidate the rate-limiting step of the hydrogenation processes shown in Figure 4D, kinetic modeling was conducted using various models (Table S1), with fitting performed over the reaction range of 0.25–0.7. Comprehensive fitting results are presented in Figures S10–S13 and Tables S2–S5 [34]. As illustrated in Figure 4E, the optimal kinetic models differ among the four CCIs. For $Ti_{50}(FeCo)_{50}$, hydrogenation is governed by a three-dimensional diffusion mechanism described by the Ginstling-Brounshtein (D4) model. In contrast, $Ti_{50}(FeCoNi)_{50}$ and $Ti_{50}(FeCoNiCuMn)_{50}$ follow a distinct three-dimensional diffusion pathway consistent with the Jander (D3) model. Meanwhile, $Ti_{50}(FeCoNiCu)_{50}$ exhibits kinetics that conform to the Johnson-Mehl-Avrami-Kolmogorov (JMAK) model with a reaction order of 1 (F1), indicating that its hydrogenation is primarily controlled by nucleation and growth of the hydride phase. In metal–hydrogen systems, the hydrogenation process typically proceeds through five successive steps. (1) Physisorption: hydrogen molecules weakly adsorb onto the metal surface through van der Waals interactions. (2) Chemisorption: the adsorbed hydrogen molecules dissociate, and the resulting atomic hydrogen forms chemical bonds with surface metal atoms. (3) Surface penetration: hydrogen atoms penetrate through the metal's surface. (4) Hydrogen diffusion: hydrogen atoms diffuse through the metal lattice. (5) Nucleation and growth of the hydride phase: the hydride phase begins nucleation, followed by growth with the interface movement. Among these steps, the slowest one limits the overall hydrogenation rate and is referred to as the rate-limiting step. Although all four CCIs have near-single-phase characters, their degree of atomic disorder, local chemical environment,

and lattice strain vary significantly. All these features may lead to different hydrogen diffusion rates, hydride phase nucleation and growth by interface movement, resulting in different kinetic behavior. For the $Ti_{50}(FeCo)_{50}$ CCI, which has the smallest atomic disorder degree, nucleation of the hydride phase is ready thus the bulk diffusion becomes the rate-limiting step. Like $Ti_{50}(FeCoNi)_{50}$ and $Ti_{50}(FeCoNiCuMn)_{50}$ CCIs follow the same model, in which the rate-limiting step is also a diffusion-controlled process. However, as the model changed from D4 to D3, this means that the addition of Ni and Mn alters the diffusion in a different geometric configuration as compared with $Ti_{50}(FeCo)_{50}$ CCI. In contrast, when introducing Cu into the B sites, as for $Ti_{50}(FeCoNiCu)_{50}$ CCI, the hydrogenation reaction is dominantly controlled by nucleation and growth of the hydride phase.

Although it will be difficult to link directly the rate-limiting steps within kinetic measurements with the thermodynamic properties of the CCIs, both the thermodynamic and kinetic behavior point to the same underlying factors related to atomic disorder, local chemical environment, and lattice distortion. Ideally, they follow the same sequence, as $Ti_{50}(FeCoNiCu)_{50}$ CCI has the least negative ΔH_{abs} and ΔS_{abs} values, and the rate-limiting step during hydrogenation is the nucleation and growth of the hydride phase. Interestingly, the introduction of Cu can introduce severe lattice distortion and greater atomic disorder, which thermodynamically weakens the metal-hydrogen bond strength and reduces structural ordering and kinetically hinders the hydride phase from continuous nucleation sites.

2.3 | Hydrogenation/Dehydrogenation Process

To track phase evolution during hydrogenation, in-situ SR-PXD was applied to $Ti_{50}(FeCo)_{50}$ under 15 bar of H_2 while ramping the temperature from 30°C to 200°C at a heating rate of 10°C min^{-1} (Figure 5A). The first emergence of hydride peaks at 2θ close to 5° appears at 136°C, marking hydride formation under this condition. In contrast, heating $Ti_{50}(FeCo)_{50}$ CCI in 1 bar of Ar with an identical temperature program produces no structural changes (Figure 5C), confirming that the new peaks in Figure 5A arise solely from hydrogen uptake. Detailed SR-PXD scans in Figure 5B,D reinforce this conclusion. Under Ar, diffraction patterns at 30°C and 136°C overlap perfectly (Figure 5D), whereas under H_2, the hydride reflections become evident alongside the parent *B2* peaks (Figure 5B). The close similarity of the hydride and *B2* lattice parameters suggests that hydrogen occupies interstitial sites without drastically distorting the host lattice.

We used high-pressure differential scanning calorimetry (DSC) to determine how atomic disorder affects the dehydrogenation activation energy (E_a). For $Ti_{50}(FeCo)_{50}$, 10 bar of H_2 was applied as back pressure, and the sample was heated from room temperature (RT) to 300°C; for the other three CCIs, the back pressure was 1 bar of H_2, and they were heated to 500°C. Note that the back pressure is different for the $Ti_{50}(FeCo)_{50}$ sample,

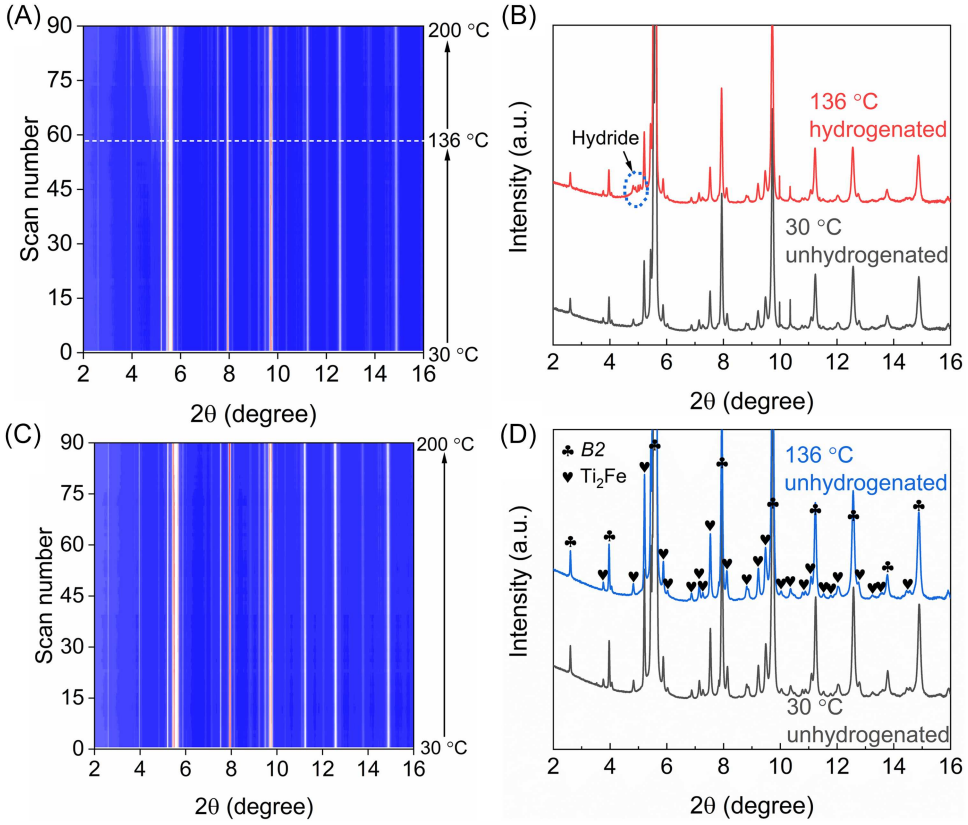

FIGURE 5 | In-situ SR-PXD analyses. (A) Two-dimensional SR-PXD map (wavelength $\lambda = 0.20739$ Å) showing phase evolution during hydrogenation of unhydrogenated $Ti_{50}(FeCo)_{50}$. (B) Phase compositions before and after hydrogenation. (C) Two-dimensional SR-PXD map of $Ti_{50}(FeCo)_{50}$ during heating in the unhydrogenated state. (D) Corresponding phase composition of unhydrogenated $Ti_{50}(FeCo)_{50}$ during thermal treatment. The data reveal structural transformations induced by hydrogen uptake and temperature variation.

as the thermodynamic stability of its hydride is higher than that of the others. Figure 6A,C,E,G display DSC traces at heating rates of 1, 3, 5°C, and 10°C min^{-1} for the hydrogenated $Ti_{50}(FeCo)_{50}$, $Ti_{50}(FeCoNi)_{50}$, $Ti_{50}(FeCoNiCu)_{50}$, and $Ti_{50}(FeCoNiCuMn)_{50}$, respectively. Under the applied conditions, $Ti_{50}(FeCo)_{50}$ exhibits two endothermic peaks, indicating a two-step dehydrogenation; its main peak temperature reaches 187.0°C at 10°C min^{-1}. At the same heating rate, the main dehydrogenation peaks are 200.9°C for $Ti_{50}(FeCoNi)_{50}$, 195.8°C for $Ti_{50}(FeCoNiCu)_{50}$, and 242.8°C for $Ti_{50}(FeCoNiCuMn)_{50}$.

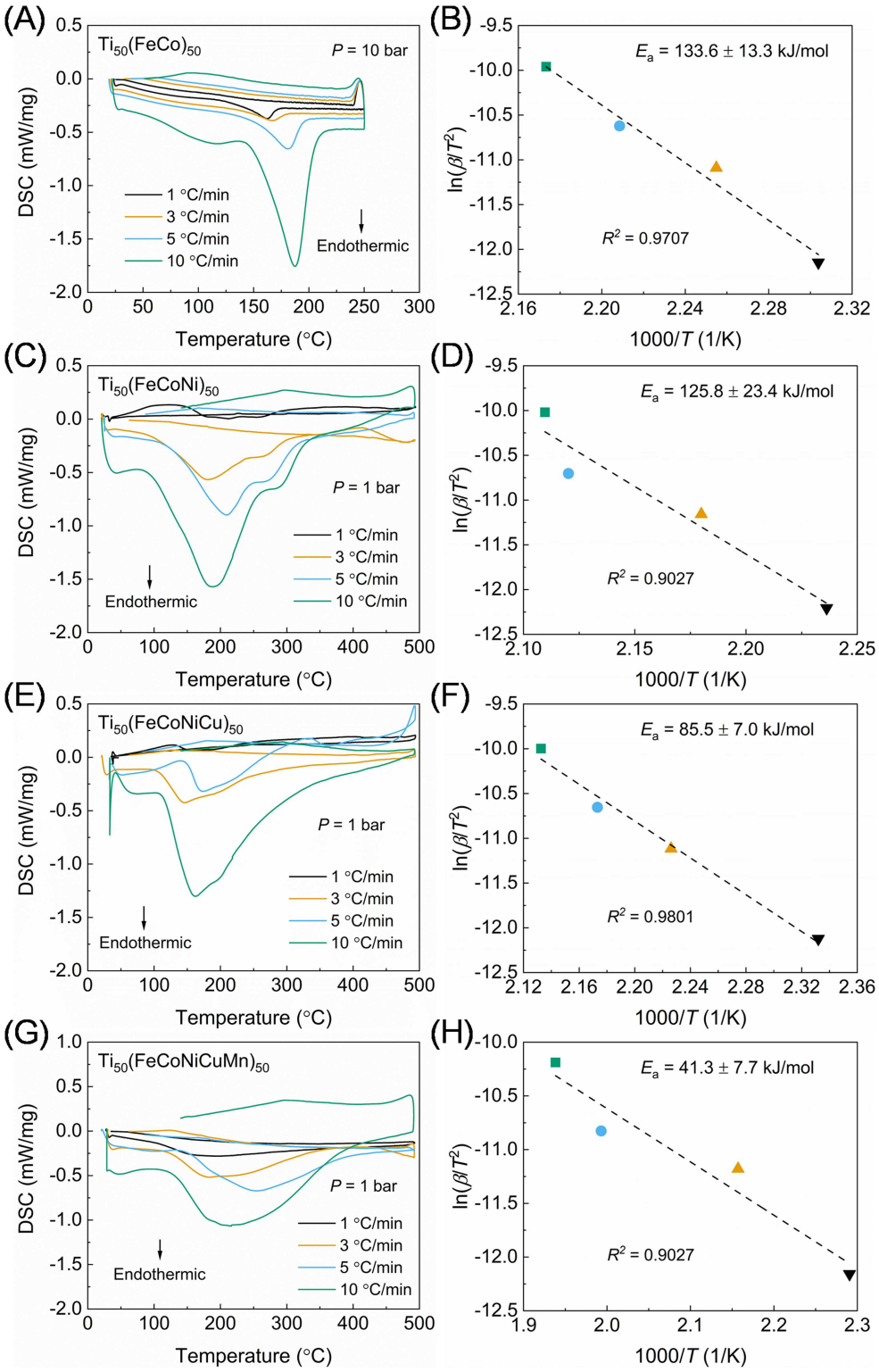

FIGURE 6 | Thermal properties of hydrogenated CCIs. (A, C, E, G) High-pressure differential scanning calorimetry (HP-DSC) curves of $Ti_{50}(FeCo)_{50}$, $Ti_{50}(FeCoNi)_{50}$, $Ti_{50}(FeCoNiCu)_{50}$, and $Ti_{50}(FeCoNiCuMn)_{50}$ CCIs at heating rates of 1, 3, 5°C, and 10°C min^{-1}. Note that the back pressure for $Ti_{50}(FeCo)_{50}$ is 10 bar of H_2, while for the other CCIs it is 1 bar of H_2. (B, D, F, H) Corresponding Kissinger plots and activation energies for the dehydrogenation process. The results provide insights into the thermal behavior and activation energies associated with hydrogen release in these CCIs.

Applying the Kissinger method (Figure 6B,D,F,H), the E_a values were extracted as 133.6 ± 13.3, 125.8 ± 23.4, 85.5 ± 7.0, and 41.3 ± 7.7 kJ mol^{-1}, respectively. These results demonstrate that dehydrogenation becomes progressively easier as the number of principal elements increases, in line with the observed kinetic trends. The observed positive effect of lattice strain on hydrogenation activity agrees with earlier reports showing that mechanically induced strain, introduced by methods such as high-pressure torsion, groove rolling, and ball milling, effectively activates TiFe-based intermetallics and improves their kinetic performances by providing fast diffusion pathways for hydrogen [13, 35, 36]. Note that the E_a values obtained from the Kissinger method can only represent the energetic barrier to overcome for the dehydrogenation process. The reaction rate also depends on the preexponential factor A, representing the entropy contributions. In this case, the differences in dehydrogenation behavior for all four CCIs may originate from different E_a and A terms, and E_a can not solely describe the kinetic performances.

2.4 | Mechanistic Insights

To understand how atomic disorder affects hydride stability, firstly, the size of the tetrahedral sites, which are preferred hydrogen locations in each *B2* lattice, was evaluated. The tetrahedral interstice radius (r_i) can be calculated using [37]:

$$r_i = \frac{-B}{2} \pm \frac{1}{2}(B^2 - 4C)^{\frac{1}{2}}, \tag{1a}$$

$$B = \frac{\sqrt{3}a}{2}, \tag{1b}$$

$$C = \frac{\frac{\sqrt{3}}{2}Ra - R^2 - \frac{a^2}{4}}{\frac{4R\sqrt{3}}{a} - \frac{8R^2}{a^2} - 1}, \tag{1c}$$

$$R = \sum_i c_i R_i, \tag{1d}$$

where a is the lattice constant, c_i and R_i are the atomic fraction and atomic radius of element i. The results indicate that r_i increases slightly from 0.3822 Å in $Ti_{50}(FeCo)_{50}$ to 0.3828 Å in $Ti_{50}(FeCoNi)_{50}$ and to 0.3848 Å in both $Ti_{50}(FeCoNiCu)_{50}$ and $Ti_{50}(FeCoNiCuMn)_{50}$. Although larger interstices generally stabilize hydrides, the PCI data at 100°C show hydride stability follows the order: $Ti_{50}(FeCo)_{50} < Ti_{50}(FeCoNiCu)_{50} < Ti_{50}(FeCoNi)_{50} < Ti_{50}(FeCoNiCuMn)_{50}$, implying additional electronic factors govern thermodynamics.

To probe these factors, DFT calculations were performed on SQS structures (128-atom bcc cells) for each composition. Convergence tests indicate that a 500 eV plane-wave cutoff energy and $6 \times 6 \times 6$/$9 \times 9 \times 9$ k-point grids for optimizations and energy calculations, respectively (Figure S14), were selected for the following calculations. Birch–Murnaghan fits to volume-energy data yielded equilibrium lattice parameters (Figure S15). Bader charge analysis (Figure 7A–D) shows Ti atoms carry Bader charges in the range of -1.1577 to -0.2226 $|e|$, indicating that Ti gains electronic density compared to neutral Ti. While Fe, Co, Ni, Cu, and Mn share similar charge states regardless of CCI complexity. The range of Ti Bader charges in the four CCIs increases with atomic disorder level, suggesting greater variations in local electronic environments and potentially more effective sites for the hydrogenation process. Figure 7E–H demonstrates the total and partial density of states (TDOSs and PDOSs) for s, p, and d orbitals of the 4 CCIs. Within the energy range of -6 to 6 eV, the d-orbits of all the CCIs contribute primarily to their TDOS curves. The Fermi level (E_f) is situated in a narrow valley for the TDOS (Figure 7I) of each CCI, hallmarking relatively structural stability. In addition, the results are in good agreement with the theory that the d-electronic orbit plays a significant role in bond formation [38]. Comparing upper d-PDOSs at E_f (Figure 7J–M) shows that the available density of electrons for bonding formation increases in the sequence: $Ti_{50}(FeCo)_{50} < Ti_{50}(FeCoNi)_{50} < Ti_{50}(FeCoNiCuMn)_{50} < Ti_{50}(FeCoNiCu)_{50}$, respectively. The activity of the surface can be quantified by the d-band center values, where a lower electron transfer efficiency is indicated by a more negative value. The upward movement of the d-band center may be a contributing factor to the strong adsorption of hydrogen because of the lower occupancy of the anti-bonding orbitals [39]. The d-band centers shift from -0.689 eV in $Ti_{50}(FeCo)_{50}$ to -0.205 eV in $Ti_{50}(FeCoNi)_{50}$, then to -0.497 eV in $Ti_{50}(FeCoNiCu)_{50}$ and -0.570 eV in $Ti_{50}(FeCoNiCuMn)_{50}$. The least negative center in $Ti_{50}(FeCoNi)_{50}$ correlates with its strongest hydrogen binding and highest plateau pressures. Element-resolved d-band projections (Figure 7J–M) show valence bands (below E_f) dominated by Fe, Co, Ni, Cu, and Mn, while conduction bands (above E_f) are Ti-rich. Introducing elements with atomic sizes that deviate significantly from the host lattice, either larger or smaller, will strain the lattice, alter orbital overlap, and tune the d-band width, that is, widest in $Ti_{50}(FeCoNi)_{50}$ and narrowest in $Ti_{50}(FeCo)_{50}$. Linking composition, interstice size, and electronic structure, especially the d-band center, offers qualitative insight into how these parameters affect hydrogen adsorption energies and tailored thermodynamics, and this may serve as a basis for guiding the design of CCIs with desired hydrogen storage properties. Nevertheless, a large number of compositions and more systematic and well-defined parameters would be necessary to establish accurate design principles. This will be investigated in future work, with the support of some advanced tools such as machine learning methods and so on.

3 | Conclusion

In this study, four CCIs with nominal compositions of $Ti_{50}(FeCo)_{50}$, $Ti_{50}(FeCoNi)_{50}$, $Ti_{50}(FeCoNiCu)_{50}$, and $Ti_{50}(FeCoNiCuMn)_{50}$ are designed to systematically investigate the effect of atomic disorder on hydrogen storage performance using both experimental and first-principles simulation methods. Under hydrogenation conditions of 100 bar at 50°C, the measured hydrogen storage capacities are 1.39, 1.42, 1.31, and 1.14 wt.% for the four CCIs, respectively. PCI analyses reveal an unexpected trend in hydride phase stability, following the sequence: $Ti_{50}(FeCoNiCuMn)_{50} > Ti_{50}(FeCoNi)_{50} > Ti_{50}(FeCoNiCu)_{50} > Ti_{50}(FeCo)_{50}$. These findings demonstrate that the thermodynamic properties of metal hydrides can be extensively tuned by adjusting the atomic disorder. Despite all four CCIs crystallizing in a nearly *B2*-type structure, as confirmed by microstructural characterization, significant differences in hydrogenation behavior are observed. DFT calculations further reveal that the influence of atomic disorder on hydrogen storage performance goes beyond configurational entropy alone, involving electronic structure

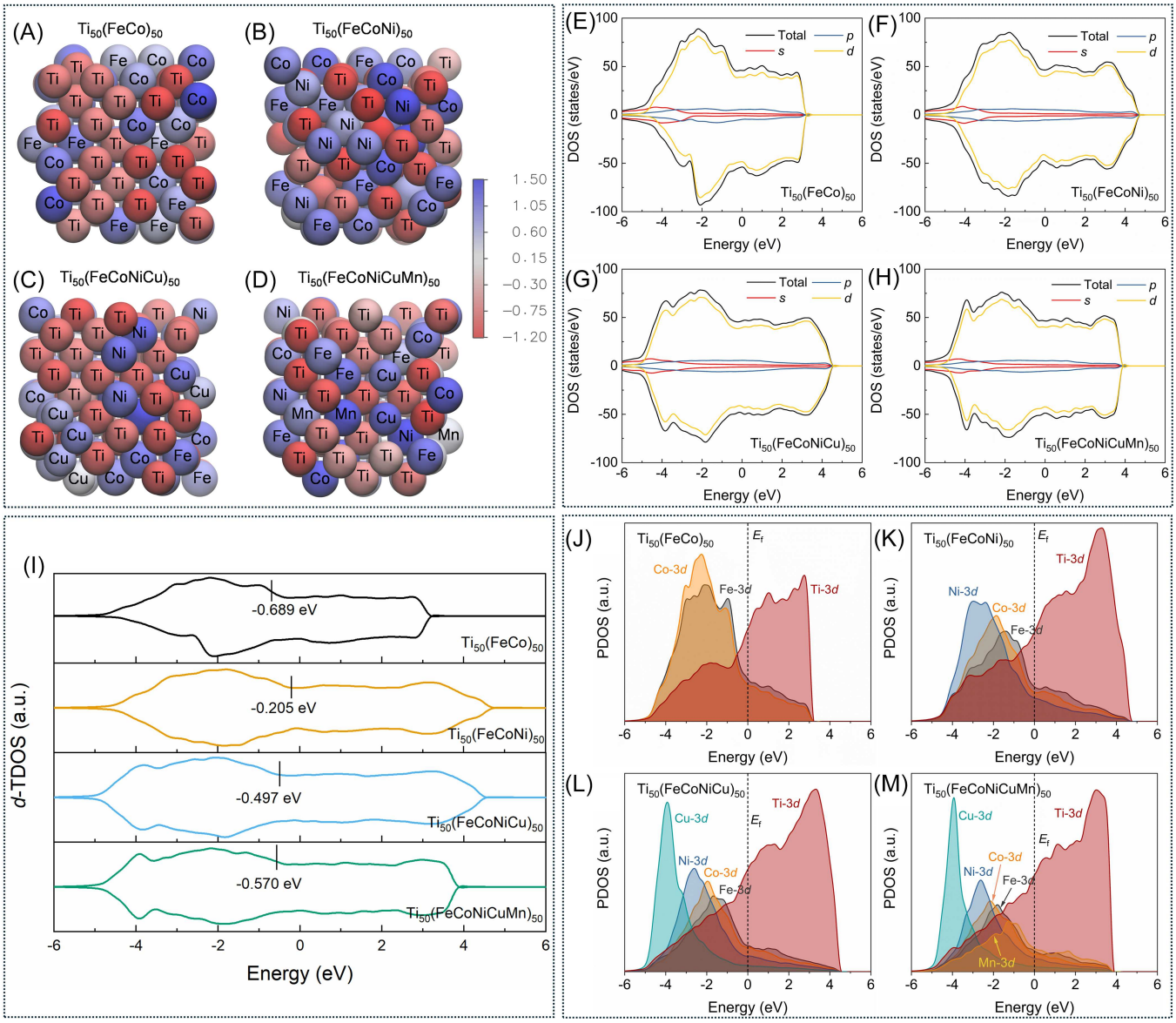

FIGURE 7 | DFT calculations. (A–D) Bader charge analysis for $Ti_{50}(FeCo)_{50}$, $Ti_{50}(FeCoNi)_{50}$, $Ti_{50}(FeCoNiCu)_{50}$, and $Ti_{50}(FeCoNiCuMn)_{50}$ CCIs. Bader charge values are in $|e|$. (E–H) TDOS and s, p, d orbital contributions for $Ti_{50}(FeCo)_{50}$, $Ti_{50}(FeCoNi)_{50}$, $Ti_{50}(FeCoNiCu)_{50}$, and $Ti_{50}(FeCoNiCuMn)_{50}$ CCIs. (I) TDOS of d-orbitals for the $Ti_{50}(FeCo)_{50}$, $Ti_{50}(FeCoNi)_{50}$, $Ti_{50}(FeCoNiCu)_{50}$, and $Ti_{50}(FeCoNiCuMn)_{50}$ CCIs. (J–M) PDOS of d-orbitals for the $Ti_{50}(FeCo)_{50}$, $Ti_{50}(FeCoNi)_{50}$, $Ti_{50}(FeCoNiCu)_{50}$, and $Ti_{50}(FeCoNiCuMn)_{50}$ CCIs. The calculations provide insights into the charge distribution and electronic structure, highlighting the contributions of different orbitals to the total density of states in the CCIs.

modifications and changes in hydrogen adsorption energetics. This work provides a foundation for the rational design of intermetallic hydrides with tailored hydrogen storage properties through compositional engineering.

4 | Experimental Section/Methods

4.1 | Materials Preparation

Commercially available Fe (99.5% purity, Alfa Aesar), Co (99.95% purity, Thermo Scientific), Ni (99.5% purity, Thermo Scientific), Cu foils (99.9% purity, Thermo Scientific), Ti (99.5% purity, Thermo Scientific), and Mn pieces (99.9% purity, Thermo Scientific) were used as starting materials. Four CCIs with nominal compositions of $Ti_{50}(FeCo)_{50}$, $Ti_{50}(FeCoNi)_{50}$, $Ti_{50}(FeCoNiCu)_{50}$, and $Ti_{50}(FeCoNiCuMn)_{50}$ (at.%) were prepared by using an Edmund Buhler MAM-1 arc melter. For each CCI, four grams of the material mixture were melted five times to ensure the homogeneity of the synthesized ingot. After melting, all the ingots were suction-casted into cylinders with a dimension of $\Phi 3 \times 30$ mm. The cylinders were hand-crushed into powders under air, and after crushing, a 125-mesh sieve was used to sieve the powders.

4.2 | Microstructural Characterizations

The SR-PXD investigations were performed at beamline P02.1 at PETRA III of DESY (Hamburg, Germany). The wavelength is 0.20735 Å, and a Varex 4343CT detector was employed. The sample-to-detector distance was calibrated using LaB_6 standard

powders from NIST. The acquired 2D images were converted to numerical data using the FIT2D program [40]. The lattice constants of each peak were calculated using Bragg's equation. Then the calculated lattice constants were displayed versus $\frac{\cos^2\theta}{2}\left(\frac{1}{\sin\theta}+\frac{1}{\theta}\right)$, where θ represents the Bragg angle. The optimal lattice constant value can be obtained by extrapolating the depicted curve to zero [41]. Phase fractions were determined using the MAUD program [42].

The in-situ SR-PXD measurements were measured at beamline P02.1 at PETRA III of DESY (Hamburg, Germany). The selected wavelength is 0.20739 Å, and the detector is a Varex 4343CT detector. The sample-to-detector distance was calibrated by using a CeO_2 standard. The acquired 2D images were converted to numerical data using the pyFAI program [43]. The conditions for the hydrogenated sample were with a back pressure of 15 bar of H_2, heating from RT to 200°C with a heating rate of 10°C min^{-1}. The conditions for the dehydrogenated sample were with 1 bar of Ar pressure, heating from RT to 200°C with a heating rate of 10°C min^{-1}.

The as-cast samples along the casting direction were prepared for analysis through standard metallographic procedures, including machining, grinding, and polishing. Microstructural characterization was performed using an FEI Quanta 650 field emission gun (FEG) SEM, equipped with an EDAX Apollo X EDS system and Velocity EBSD detectors. The data from EBSD was analyzed by TSL OIM 8.

4.3 | Hydrogen Storage Property Analyses

Prior to hydrogen storage property analyses, the CCI powders obtained by sieving were activated. The activation was performed by varying pressure and temperature, as described in a previous work [8]. After that, all the handling of the activated powders were done inside an Ar-filled glovebox (both O_2 and H_2O levels ≤ 1 ppm). To obtain the thermodynamic properties of the CCIs, a GASPRO Sieverts-type gas sorption analyzer was utilized to measure the hydrogenation and dehydrogenation PCI curves of each activated sample (50, 75, 100, and 125°C for $Ti_{50}(FeCo)_{50}$; whereas 50, 100, 150, and 200°C for $Ti_{50}(FeCoNi)_{50}$, $Ti_{50}(FeCoNiCu)_{50}$, and $Ti_{50}(FeCoNiCuMn)_{50}$). Approximately 2 g of each CCI was placed into a steel sample vial and closed with a screw lid containing porous sintered metal filters. The steel sample vial was then inserted into an autoclave-style sample holder (maximum temperature of 400°C and maximum pressure of 200 bar). The selected hydrogen pressure step is in the range of 3 to 5 bar, while the equilibrium time is about 60 to 120 min for each pressure step. The measured pressure ranges from 0 to 100 bar of H_2. The van't Hoff equation was used to calculate the hydrogenation and dehydrogenation ΔH and ΔS:

$$\ln\frac{P_{eq}}{P_0}=\frac{\Delta H}{RT}-\frac{\Delta S}{R}, \tag{2}$$

where P_{eq} is the equilibrium pressure obtained from the PCI measurements, P_0 is the standard pressure, R is the gas constant, and T is the sample temperature. The ΔH and ΔS can be obtained from the slope and the y-intercept by applying linear fitting of $\ln\frac{P_{eq}}{P_0}$ versus $\frac{1}{T}$.

The kinetic properties of the CCIs were investigated on a custom-built in-house Sieverts-type apparatus. The hydrogenation measurements were conducted under 50 bar of H_2 at 50°C. The conditions for dehydrogenation measurements are as follows: under 0.5 bar of H_2, heating from 50°C to 300°C with a heating rate of 10°C min^{-1}.

4.4 | Thermal Analyses

Thermal analyses of the dehydrogenation via DSC were performed on an HP-DSC 204 HP Phoenix from Netzsch, located in an Ar-filled glovebox with O_2 and H_2O levels less than 1 ppm. For measurements, approximately 20 mg of the sample were placed into an Al_2O_3 crucible on the sample side, with the same type of crucible on the reference side. The hydrogenated $Ti_{50}(FeCo)_{50}$ sample was heated from RT to 250°C under 10 bar of H_2 pressure. For the other three hydrogenated samples, they were heated from RT to 500°C under 1 bar of H_2 pressure. To calculate the E_a of the dehydrogenation process by the Kissinger method, varying heating rates were applied (1, 3, 5, and 10°C min^{-1}):

$$\ln\frac{\beta}{{T_{max}}^2}=-\frac{E_a}{RT_{max}}+\ln\frac{AR}{E_a}, \tag{3}$$

where T_{max} is the peak temperature for the dehydrogenation event, β is the corresponding heating rate, and A is the pre-exponential factor.

4.5 | Computational Methods

The first-principles calculations were carried out via DFT as implemented in the Vienna *Ab-initio* Simulation Package (VASP) version 5.4.4 [44, 45]. The exchange-correlation interactions were described using the revised version of the Perdew-Burke-Ernzerhof functional for solids and surfaces (PBESol) within the generalized gradient approximation (GGA) [46, 47]. The Monte Carlo SQS (MCSQS) tool within the Alloy Theory Automation Toolkit (ATAT) was utilized to generate SQS of CCIs. For each composition, the structure with relative stability was selected [48]. All structures were constructed adopting a bcc lattice including 128 atoms. All calculations took spin polarization into account. The structural relaxations were performed using ISIF = 2, with an energy convergence criterion of 1×10^{-5} eV $atom^{-1}$, until the residual forces on all atoms fell below 0.01 eV $Å^{-1}$. The Brillouin zone integrations for optimization and energy calculations were conducted using Gamma-centered k-meshes of $(6\times6\times6)$ and $(9\times9\times9)$, respectively. The analyses of electronic properties were done with the Bader charge analysis and VASPKIT program [49, 50].

Acknowledgments

This research was partially funded by dtec. bw—Digitalization and Technology Research Center of Bundeswehr, which we gratefully acknowledge. Dr. Zhifeng Lei would like to acknowledge funding from the National Natural Science Foundation of China (No. 52371153),

the Fundamental Research Funds for the Central Universities (No. 531118010621), and the National Natural Science Foundation of Hunan Province (No. 2025JJ30017). We acknowledge DESY (Hamburg, Germany), a member of the Helmholtz Association HGF, for the provision of experimental facilities. Parts of this research were carried out at PETRA III, and we would like to thank Dr. Alexander Schökel, Dr. Martin Aaskov Karlsen, and Dr. Morten Johansen for assistance in using photon beamline P02.1. Beamtime was allocated for proposals I-20220883 and BAG-20240008. Open Access funding enabled and organized by Projekt DEAL.

Conflicts of Interest

The authors declare no conflicts of interest.

References

1. E. Tzimas, C. Filiou, S. D. Peteves, and J. B. Veyret, "Hydrogen Storage: State-of-the-Art and Future Perspective," EU Commission, JRC Petten, EUR 20995EN. 2003.

2. P. Chen and M. Zhu, "Recent Progress in Hydrogen Storage," *Materials Today* 11 (2008): 36–43.

3. A. Schneemann, J. L. White, S. Kang, et al., "Nanostructured Metal Hydrides for Hydrogen Storage," *Chemical Reviews* 118 (2018): 10775–10839.

4. Y. Wang, Y. Xue, and A. Züttel, "Nanoscale Engineering of Solid-State Materials for Boosting Hydrogen Storage," *Chemical Society Reviews* 53 (2024): 972–1003.

5. Y. Cho, A. J. E. Rowberg, S. Chatterjee, et al., "Chemical Redox Agent-Driven Noncorrosive Formation of Nanoporous Mg Structures for Advanced Hydrogen Storage," *ACS Nano* 19 (2025): 5649–5658.

6. X. Y. Wang, P. Peng, M. D. Witman, V. Stavila, M. D. Allendorf, and H. M. Breunig, "Technoeconomic Insights Into Metal Hydrides for Stationary Hydrogen Storage," *Advancement of Science* 12 (2025): 2415736.

7. Y. Zhang, C. Li, Z. Yuan, Y. Qi, S. Guo, and D. Zhao, "Research Progress of TiFe-Based Hydrogen Storage Alloys," *Journal of Iron and Steel Research International* 29 (2022): 537–551.

8. Y. Shang, S. Liu, Z. Liang, et al., "Developing Sustainable FeTi Alloys for Hydrogen Storage by Recycling," *Communications Materials* 3 (2022): 101.

9. V. Y. Zadorozhnyy, S. N. Klyamkin, M. Y. Zadorozhnyy, O. V. Bermesheva, and S. D. Kaloshkin, "Mechanical Alloying of Nanocrystalline Intermetallic Compound TiFe Doped by Aluminum and Chromium," *Journal of Alloys and Compounds* 586 (2014): S56–S60.

10. Y. Li, H. Shang, Y. Zhang, P. Li, Y. Qi, and D. Zhao, "Investigations on Gaseous Hydrogen Storage Performances and Reactivation Ability of As-Cast $TiFe_{1-x}Ni_x$ ($x = 0$, 0.1, 0.2 and 0.4) Alloys," *International Journal of Hydrogen Energy* 44 (2019): 4240–4252.

11. E. M. Dematteis, N. Berti, F. Cuevas, M. Latroche, and M. Baricco, "Substitutional Effects in TiFe for Hydrogen Storage: A Comprehensive Review," *Materials Advances* 2 (2021): 2524–2560.

12. E. M. Dematteis, D. M. Dreistadt, G. Capurso, J. Jepsen, F. Cuevas, and M. Latroche, "Fundamental Hydrogen Storage Properties of TiFe-Alloy With Partial Substitution of Fe by Ti and Mn," *Journal of Alloys and Compounds* 874 (2021): 159925.

13. H. Emami, K. Edalati, J. Matsuda, E. Akiba, and Z. Horita, "Hydrogen Storage Performance of TiFe After Processing by Ball Milling," *Acta Materialia* 88 (2015): 190–195.

14. T. Suda, M. Ohkawa, S. Sawada, S. Watanabe, S. Ohnuki, and S. Nagata, "Effect of Surface Modification by Ion Implantation on Hydrogenation Property of TiFe Alloy," *Materials Transactions* 43 (2002): 2703–2705.

15. L. E. R. Vega, D. R. Leiva, R. M. Leal Neto, et al., "Mechanical Activation of TiFe for Hydrogen Storage by Cold Rolling Under Inert Atmosphere," *International Journal of Hydrogen Energy* 43 (2018): 2913–2918.

16. Z. Yuan, Y. Sui, Q. Yuan, et al., "Effects of Ball Milling Time on the Microstructure and Hydrogen Storage Performances of $Ti_{21.7}Y_{0.3}Fe_{16}Mn_3Cr$ Alloy," *International Journal of Hydrogen Energy* 48 (2023): 11340–11351.

17. J. W. Yeh, S. K. Chen, S. J. Lin, et al., "Nanostructured High-Entropy Alloys With Multiple Principal Elements: Novel Alloy Design Concepts and Outcomes," *Advanced Engineering Materials* 6 (2004): 299–303.

18. B. Cantor, I. T. H. Chang, P. Knight, and A. J. B. Vincent, "Microstructural Development in Equiatomic Multicomponent Alloys," *Materials Science and Engineering: A* 375–377 (2004): 213–218.

19. E. P. George, D. Raabe, and R. O. Ritchie, "High-Entropy Alloys," *Nature Reviews Materials* 4 (2019): 515–534.

20. J. T. Ren, L. Chen, H. Y. Wang, and Z. Y. Yuan, "High-Entropy Alloys in Electrocatalysis: From Fundamentals to Applications," *Chemical Society Reviews* 52 (2023): 8319–8373.

21. S. Schweidler, M. Botros, F. Strauss, et al., "High-Entropy Materials for Energy and Electronic Applications," *Nature Reviews Materials* 9 (2024): 266–281.

22. Z. Li, R. Wu, D. Duan, et al., "Empowering Multicomponent Alloys With Unique Nanostructure for Exceptional Oxygen Evolution Performance Through Self-Replenishment," *Joule* 8 (2024): 2920–2937.

23. Z. W. Chen, J. Li, P. Ou, et al., "Unusual Sabatier Principle on High Entropy Alloy Catalysts for Hydrogen Evolution Reactions," *Nature Communications* 15 (2024): 359.

24. L. He, M. Li, L. Qiu, et al., "Single-Atom Mo-Tailored High-Entropy-Alloy Ultrathin Nanosheets With Intrinsic Tensile Strain Enhance Electrocatalysis," *Nature Communications* 15 (2024): 2290.

25. H. Luo, Z. Pan, T. Yang, et al., "A High-Entropy Alloy for Superior Resistance to Biogenic Sulfuric Acid Corrosion and Hydrogen Embrittlement," *Matter* 8 (2025): 101944.

26. S. Dangwal and K. Edalati, "High-Entropy Alloy $TiV_2ZrCrMnFeNi$ for Hydrogen Storage at Room Temperature With Full Reversibility and Good Activation," *Scripta Materialia* 238 (2024): 115774.

27. S. Dangwal, Y. Ikeda, B. Grabowski, and K. Edalati, "Machine Learning to Explore High-Entropy Alloys With Desired Enthalpy for Room-Temperature Hydrogen Storage: Prediction of Density Functional Theory and Experimental Data," *Chemical Engineering Journal* 493 (2024): 152606.

28. C. Guan, X. Yue, and Q. Xiang, "The Role of Lattice Distortion in Catalysis: Functionality and Distinctions From Strain," *Advanced Materials* 37 (2025): 2501209.

29. R. Kirchheim, "Diffusion of Hydrogen and Other Interstitials in Disordred and Amorphous Materials," *Defect and Diffusion Forum* 143 (1997): 911–926.

30. Z. Ding, Y. Li, H. Jiang, et al., "The Integral Role of High-Entropy Alloys in Advancing Solid-State Hydrogen Storage," *Interdisciplinary Materials* 4 (2025): 75–108.

31. H. Kim, S. Kang, J. Y. Lee, et al., "A New Perspective on the Initial Hydrogenation of $TiFe_{0.9}M_{0.1}$ (M = V, Cr, Fe, Co, Ni) Alloys Gained From Surface Oxide Analyses and Nucleation Energetics," *Applied Surface Science* 610 (2023): 155443.

32. G. K. Sujan, Z. Pan, H. Li, D. Liang, and N. Alam, "An Overview on Tife Intermetallic for Solid-State Hydrogen Storage: Microstructure, Hydrogenation and Fabrication Processes," *Critical Reviews in Solid State and Materials Sciences* 45 (2020): 410–427.

33. A. Santhosh, S. Kang, N. Keilbart, et al., "Influence of Near-Surface Oxide Layers on TiFe Hydrogenation: Mechanistic Insights and

Implications for Hydrogen Storage Applications," *Journal of Materials Chemistry A* 11 (2023): 18776–18789.

34. A. Khawam and D. R. Flanagan, "Solid-State Kinetic Models: Basics and Mathematical Fundamentals," *Journal of Physical Chemistry B* 110 (2006): 17315–17328.

35. K. Edalati, J. Matsuda, A. Yanagida, E. Akiba, and Z. Horita, "Activation of TiFe for Hydrogen Storage by Plastic Deformation Using Groove Rolling and High-Pressure Torsion: Similarities and Differences," *International Journal of Hydrogen Energy* 39 (2014): 15589–15594.

36. K. Edalati, M. Matsuo, H. Emami, et al., "Impact of Severe Plastic Deformation on Microstructure and Hydrogen Storage of Titanium-Iron-Manganese Intermetallics," *Scripta Materialia* 124 (2016): 108–111.

37. C. E. Lundin, F. E. Lynch, and C. B. Magee, "A Correlation Between the Interstitial Hole Sizes in Intermetallic Compounds and the Thermodynamic Properties of the Hydrides Formed From Those Compounds," *Journal of the Less Common Metals* 56 (1977): 19–37.

38. D. Kuroda, M. Niinomi, M. Morinaga, Y. Kato, and T. Yashiro, "Design and Mechanical Properties of New β Type Titanium Alloys for Implant Materials," *Materials Science and Engineering: A* 243 (1998): 244–249.

39. F. Kong, X. Liu, Y. Song, et al., "Selectively Coupling Ru Single Atoms to PtNi Concavities for High-Performance Methanol Oxidation via d-Band Center Regulation," *Angewandte Chemie International Edition* 61 (2022): e202207524.

40. A. P. Hammersley, "FIT2D: An Introduction and Overview," *European Synchrotron Radiation Facility Internal Report ESRF97HA02T* 68 (1997): 58.

41. J. B. Nelson and D. P. Riley, "An Experimental Investigation of Extrapolation Methods in the Derivation of Accurate Unit-Cell Dimensions of Crystals," *Proceedings of the Physical Society* 57 (1945): 160–177.

42. L. Lutterotti, S. Matthies, and H. R. Wenk, "MAUD: A Friendly Java Program for Material Analysis Using Diffraction," *IUCr: Newsletter of the CPD* 21 (1999): 14–15.

43. G. Ashiotis, A. Deschildre, Z. Nawaz, et al., "The Fast Azimuthal Integration Python Library," *Journal of Applied Crystallography* 48 (2015): 510–519.

44. G. Kresse and J. Furthmüller, "Efficiency of *Ab-Initio* Total Energy Calculations for Metals and Semiconductors Using a Plane-Wave Basis Set," *Computational Materials Science* 6 (1996): 15–50.

45. G. Kresse and J. Furthmüller, "Efficient Iterative Schemes for *Ab Initio* Total-Energy Calculations Using a Plane-Wave Basis Set," *Physical Review B* 54 (1996): 11169–11186.

46. J. P. Perdew, A. Ruzsinszky, G. I. Csonka, et al., "Restoring the Density-Gradient Expansion for Exchange in Solids and Surfaces," *Physical Review Letters* 100 (2008): 136406.

47. J. P. Perdew, K. Burke, and M. Ernzerhof, "Generalized Gradient Approximation Made Simple," *Physical Review Letters* 77 (1996): 3865–3868.

48. A. van de Walle, P. Tiwary, M. de Jong, et al., "Efficient Stochastic Generation of Special Quasirandom Structures," *Calphad* 42 (2013): 13–18.

49. G. Henkelman, A. Arnaldsson, and H. Jónsson, "A Fast and Robust Algorithm for Bader Decomposition of Charge Density," *Computational Materials Science* 36 (2006): 354–360.

50. V. Wang, N. Xu, J. C. Liu, G. Tang, and W. T. Geng, "VASPKIT: A User-Friendly Interface Facilitating High-Throughput Computing and Analysis Using VASP Code," *Computer Physics Communications* 267 (2021): 108033.

Supporting Information

Additional supporting information can be found online in the Supporting Information section.
Supplementary Materials-final.